

Physical and electrical properties of combustion synthesized NASICON type $\text{Na}_3\text{Cr}_2(\text{PO}_4)_3$ crystallites: Effect of glycine molar ratios

Lakshmi Vijayan^a, Rajesh Cheruku^a, G. Govindaraj^{a,*}, S. Rajagopan^b

^a Department of Physics, School of Physical, Chemical and Applied Sciences, Pondicherry University, R.V. Nagar, Kalapet, Pondicherry 605 014, India

^b Department of Chemistry, Pondicherry Engineering College, Pondicherry 605 014, India

ARTICLE INFO

Article history:

Received 2 December 2010

Received in revised form 16 July 2011

Accepted 7 August 2011

Keywords:

Nanocrystalline

Chemical synthesis

Electrical conductivity

Electrical properties

ABSTRACT

Thermally stable $\text{Na}_3\text{Cr}_2(\text{PO}_4)_3$ nano-crystallites are synthesized through novel solution combustion technique using glycine fuel in three molar ratios. Effects of fuel molar ratio on structural and electrical properties are investigated. Reaction parameters like fuel molar ratio, flame temperature and number of moles of gases evolved, play a major role in deciding physical and electrical properties. Out of the synthesized samples, one which contains fuel in 1:1 molar ratio shows highest grain conductivity of $2.35 \times 10^{-6} \text{ S cm}^{-1}$. Improved conductivity is elucidated by least size and highest density of the crystallites, which in turn is decided by the flame temperature. Ac electrical properties are investigated using complex impedance spectroscopy. Activation energies for dc conduction and relaxation are determined and the results are reported.

© 2011 Elsevier B.V. All rights reserved.

1. Introduction

NASICON type materials are potentially important in solid state ionic devices due to its application as solid electrolytes. High ionic conductivity and stability of phosphate units are advantages of NASICON over other electrolyte materials [1]. In the frame-work, $\text{A}_x\text{B}_y(\text{PO}_4)_3$, A is an alkali metal ion and B is a multivalent metal ion. The charge compensating A cations occupy two types of sites, M1 and M2 (1:3 multiplicity), in interconnected channels formed by corner sharing PO_4 tetrahedra and BO_6 octahedra. M1 sites are surrounded by six oxygens and located at an inversion center and M2 sites are symmetrically distributed around three-fold axis of the structure with ten-fold oxygen coordination. In three-dimensional frame-work of NASICON, numerous ionic substitutions are allowed at various lattice sites [2]. Typically, NASICON type materials are stable in rhombohedral symmetry with $R\bar{3}c$ space group. But micro-crystalline NASICON, containing Cr and Fe in B site exhibit structural phase transition and crystallized in less stable monoclinic symmetry [3]. While, the same phase synthesized through chemical route [4] persists in stable symmetry. High ion conducting structurally-stable NASICON material has enormous application in solid state devices. Especially, Na^+ ion conducting NASICON is widely used in CO_2 and SO_x sensors because of its ion-sensitivity, and these materials exhibit good response and excellent selectivity against CO_2 and NO_2 . The $\text{Na}_3\text{Cr}_2(\text{PO}_4)_3$ could be a possible material for

sensor application owing to its conductivity and thermally stable structure.

Different preparation techniques exist to reduce the size of crystallites; among those hydrothermal, sol-gel and co-precipitation are commonly used for NASICON synthesis [5–7]. Even though these methods have several advantages in terms of homogeneity and fine particle nature; it is difficult to obtain phase pure material by these methods. An alternate approach is solution combustion technique; few reports are available on the synthesis of NASICON by this technique [8]. Self-propagating combustion synthesis works on the principle of decomposition of an oxidizing agent (metal nitrate), in the presence of reducing agents like urea, citric acid and glycine. This redox reaction completes in short time followed by rapid cooling leading to nucleation without the growth of crystallites. Gas evolution during combustion promotes formation of pores, which disintegrates large particles or agglomerates and high purity products are formed.

A few studies reported the correlation between synthesis parameters and electrical properties of NASICON material. In the present study, exertion has been made to ascertain the implication of fuel molar ratio on structural and electrical relaxation dynamics of $\text{Na}_3\text{Cr}_2(\text{PO}_4)_3$ crystallites. Glycine, one of the smallest amino acids with the formula $\text{NH}_2\text{CH}_2\text{COOH}$, is used as the reducing/complexing agent in different molar ratios 1:1, 1:2 and 1:3 in this study. Fuel molar ratio is an important aspect in deciding the structural parameters and electrical relaxation dynamics of the material. Different characterization tools like X-ray diffraction (XRD), Fourier-transform infrared spectroscopy (FTIR), UV-vis spectroscopy, Thermo-gravimetry and differential thermal analysis (TG-DTA), Scanning electron microscopy (SEM) and Transmission

* Corresponding author. Tel.: +91 413 2654405; fax: +91 413 2655183.

E-mail address: ggraj.7@yahoo.com (G. Govindaraj).

Table 1
Thermodynamic data of reactants and products.

Compound	ΔH_f^0 (Kcal mol ⁻¹)	C_p (Kcal mol ⁻¹ K ⁻¹)
Na ₃ Cr ₂ (PO ₄) ₃	-467.05	346.60
NaNO ₃	-111.81	–
Cr(NO ₃) ₃ ·9H ₂ O	-823.13	–
NH ₄ H ₂ PO ₄	-341.48	–
H ₂ O ^g	-57.79	33.59
CO ₂ ^g	-94.05	37.13
N ₂ ^g	–	29.12
O ₂ ^g	–	29.37
NH ₂ CH ₂ COOH	-126.31	–

electron microscopy (TEM) are explored for structural studies. For exposition of ac electrical relaxation, electrical parameters are investigated in the frequency range of 10 Hz–25 MHz at different temperatures and the results are reported.

2. Experimental details

Stoichiometric amount of NaNO₃, Cr(NO₃)₃·9H₂O, NH₄H₂PO₄ and glycine were mixed in required molar ratios in minimum volume of deionized water. The resulting solution after homogenous mixing and thermal dehydration in a magnetic stirrer became viscous liquid. Temperature was increased to 100 °C for auto-ignition with rapid evolution of large volume of gases to produce voluminous powder, named to be as-prepared material. The nature of ignition depends on fuel molar ratio and combustion was more powerful for large molar ratios.

Before carrying out electrical measurements, pellets were sintered at 900 °C for 24 h and at 1150 °C for 3 h. Silver paint was evenly applied on both sides of pellets for better electrical contact. Ac electrical measurements were carried out by two terminal method using PSM 1735 LCZ meter in the temperature range from 373 K to 503 K where complex impedance, phase angle, conductance (G) and capacitance (C) were measured.

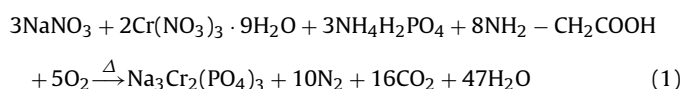
The ion transport number was measured by dc polarization technique. In this technique, a dc voltage of 400 mV is applied across the sample kept between a pair of blocking silver electrodes. The resulting polarization current through the circuit was measured as a function of time using Keithley 238 high current source measure unit.

Powder XRD patterns were recorded at room temperature using Philips X'pert PRO diffractometer in the 2θ range of 5°–75°. High temperature XRD measurements were carried out using Anton par HT attachment. TG and DTA measurements were carried out using TG-DTA instrument Model: Q600 SDT from TA instruments in the temperature range of 40–1000 °C. FTIR spectra were recorded using Thermo Nicolet made FTIR spectrometer of Model: 6700. Spectrum was recorded between 400 cm⁻¹ and 1400 cm⁻¹ using KBr as diluter and UV–vis spectrum was recorded using Ocean optics HR4000 in the range of 200–1100 nm. Scanning transmission electron microscopy (SEM) and transmission electron microscopy (TEM) were employed to distinguish the surface morphology and crystallite size of the products. SEM was recorded using model S-3400 from Hitachi and TEM using JEOL 2100F.

3. Results and discussions

Glycine plays dual role in combustion reaction; being a carboxylic group at one end and an amino group at other end, it can behave as zwitterion. Both end of which can take part in complexation of metal ions of varying sizes, which helps in preventing selective precipitation to maintain compositional homogeneity among the constituents. Metal nitrates are reduced by glycine through an exothermic redox reaction during combustion and the adiabatic flame temperature reach above 1000 °C depending on the fuel ratio.

In the case of glycine–nitrate combustion, primarily N₂, CO₂, and H₂O are evolved as gaseous products [9]. Over all reaction for formation of Na₃Cr₂(PO₄)₃ using glycine in 1:1 fuel ratio (denoted as Na₃Cr₂(PO₄)₃-G1:1) is given by,



Adiabatic flame temperature for the reaction in Eq. (1), is calculated using thermodynamic data given in Table 1. The enthalpy of combustion can be expressed as:

$$\Delta H^0 = \left(\sum n \Delta H_f^0 \right)_{\text{products}} - \left(\sum n \Delta H_f^0 \right)_{\text{reactants}}$$

and

$$\Delta H^0 = \int_{298}^{T_f} \left(\sum n C_p \right)_{\text{products}} dT \quad (2)$$

where n is the number of moles, T_f is the adiabatic flame temperature and C_p is the heat capacity (constant pressure) of products. Adiabatic flame temperature is estimated by using the equation:

$$T_f = \frac{T_0 + \Delta H^0}{C_p} \quad (3)$$

where T_0 is the initiation temperature and T_f is the maximum combustion temperature achieved under adiabatic conditions. The adiabatic flame temperature for 1:1 fuel molar ratio turns out to be 1509 K from Eq. (3) and as expected the flame temperature increases substantially with fuel ratio. However, actual flame temperature is much lower than the theoretical value due to radiative losses, incomplete combustion and heating of air [10]. The powder characteristics, namely, crystallite size and surface area are primarily governed by enthalpy or flame temperature during combustion, where the flame temperature depends on nature of the fuel and its fuel molar ratio [11]. Rapid evolution of large volume of gaseous products during combustion dissipates heat during combustion whereby limits the growth of temperature. This reduces the possibility of premature local partial sintering among primary particles. The gas evolution helps in limiting the inter-particle contact.

As-prepared material is in amorphous form and the XRD patterns of sintered Na₃Cr₂(PO₄)₃ at 900 °C are shown in Fig. 1(a). The spectra match well with JCPDS data reference number 01-077-0748, which is in rhombohedral crystal system with R3c space group. Crystallite size is calculated from Williamson–Hall plot between $B \cos \theta$ and $4 \sin \theta$, using XRD data. The Williamson–Hall [12] equation is:

$$B \cos \theta = \frac{K\lambda}{D} + 4\epsilon \sin \theta \quad (4)$$

where B is the full width at half maximum (FWHM), θ is the Bragg angle, K is the Scherrer constant, D is the crystallite size, λ is the wavelength of X-ray, ϵ is the lattice strain. For Gaussian X-ray profiles, B can be calculated as: $B^2 = B_m^2 - B_s^2$ where B_m is the FWHM measured for specimen, B_s is the FWHM of silicon standard, which is used to eliminate instrumental broadening. Using a linear interpolation to Williamson–Hall plot, intercept give crystallite size.

The crystallite size is decided mainly by two factors i.e. adiabatic flame temperature and number of moles of gases released during combustion. The flame temperature and the number of moles of gases released are more for large fuel ratio. High values of flame-temperature result in the formation of dense agglomerates that are disintegrated by the release of large amount of gases [13]. Hence, competition between flame temperature and number of moles of gases released decides the crystallite size. Crystallites of Na₃Cr₂(PO₄)₃-G1:1 are the smallest among the three fuel ratios and Table 2 shows variation of crystallite size. From these observations, present study signifies that the flame temperature has more effect on controlling the crystallite size than the number of moles of gases released during combustion. Density of sintered pellets is measured through Archimedes' method using xylene as solvent. Table 2 shows the variation in the density of samples. All the materials were sintered more than 90% of its theoretical density. Among the materials of different fuel molar ratios, Na₃Cr₂(PO₄)₃-G1:1 has the highest density due to close packing of smallest crystallites

Table 2

Lattice parameters are calculated by refinement of XRD pattern using GSAS software. Average crystallite size is calculated from the Williamson–Hall plot.

Sample	Lattice parameters				Density of sintered pellet ($\pm 1.23\%$)	Volume (\AA^3)	Crystallite (nm)
	$a(=b)$ (\AA)	c (\AA)	α	γ			
NCP-G1:1	8.637 (4)	21.615 (1)	90.00	120.00	93.25%	1396.53 (5)	31.29 ± 3.91
NCP-G1:2	8.656 (7)	21.675 (6)	90.00	120.00	91.49%	1406.72 (8)	34.02 ± 2.68
NCP-G1:3	8.657 (4)	21.681 (7)	90.00	120.00	90.89%	1407.36 (6)	39.39 ± 4.12

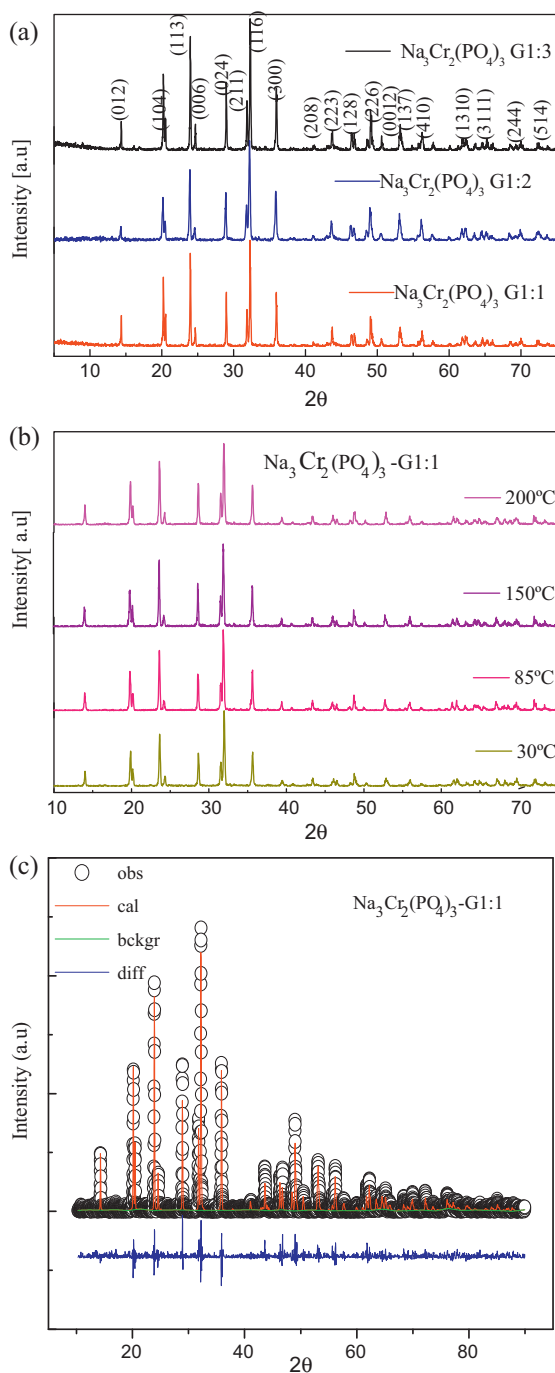


Fig. 1. (a) XRD pattern of $\text{Na}_3\text{Cr}_2(\text{PO}_4)_3$ in three fuel molar ratios calcined at 900°C . (b) XRD pattern of $\text{Na}_3\text{Cr}_2(\text{PO}_4)_3\text{-G1:1}$ at 30°C , 85°C , 150°C and 200°C . (c) Rietveld refinement showing observed, calculated and difference XRD pattern of $\text{Na}_3\text{Cr}_2(\text{PO}_4)_3\text{-G1:1}$ calcined at 900°C .

[14]. When compared to solid state synthesis, solution combustion method enables dense sintering of materials at lower temperature. The reduction in sintering temperature of solution combustion method may be explained based on the enhanced kinetics due to the ultrafine nature of the nanostructured material.

Microcrystalline NASICON containing Cr and Fe in B site lattices are not thermally stable. It shows transitions from room temperature α -form to α' at 75°C , $\alpha' \rightarrow \beta$ at 138°C and $\beta \rightarrow \gamma$ at 166°C . α -form is in monoclinic phase with superstructure reflections, where Na^+ ions are located at M1 sites in ordered manner [3]. In rhombohedral phase of γ -form, Na^+ ions are distributed on available M1 and M2 sites in disordered manner. While, $\text{Na}_3\text{Cr}_2(\text{PO}_4)_3$ nano-crystallites synthesized by this novel technique crystallized in thermally stable rhombohedral phase. This sort of structural modification is common in materials synthesized by various chemical routes [3].

In order to confirm the structural stability, XRD patterns of $\text{Na}_3\text{Cr}_2(\text{PO}_4)_3\text{-G1:1}$ is recorded at 30 , 85 , 150 and 200°C . The high temperature patterns match well with the room temperature pattern as shown in Fig. 1(b). To confirm the phase, Rietveld refinement of $\text{Na}_3\text{Cr}_2(\text{PO}_4)_3\text{-G1:1}$ is performed using GSAS computer package [15,16]. In Fig. 1(c), symbol shows experimental data collected in slow scan mode; calculated and difference patterns are in solid lines of different colors. Refinement is performed based on rhombohedral crystal system with $R\bar{3}c$ space group. The parameters like zero shift, unit-cell parameters, FWHM, background, scale factor and pseudo-voigt coefficient are refined initially. Then lattice parameters, atomic positions of Cr, P and O are refined in $12c$ ($0, 0, z$), $18e$ ($x, 0, 1/4$), and $36f$ (x, y, z) Wyckoff positions, respectively. Na^+ is assumed to occupy M1 site and M2 site partially; whose Wyckoff positions are $6b$ ($0, 0, 0$) and $18e$ ($x, 0, 1/4$) respectively and results are given in Table 3.

Thermal and gravimetric analyses of as-prepared materials are carried out in the temperature range of 40 – 1000°C . This study confirms the structural phase change in materials and enthalpy of products can be calculated from area of crystallization peak. TG-DTA curve of as-prepared samples are shown in Fig. 2(a)–(c). Out of the two exothermic peaks observed in DTA, first broad peak is around 200 – 400°C and the second sharp peak is around 740 – 780°C . The former peak indicates decomposition of organic fuel and nitrates producing NH_3 and NO_2 gases, which activate main combustion reaction; while the latter corresponds to the burning of residual organic matter and its subsequent crystallization. The gravimetric plot shows significant weight loss in the temperature range of 300 – 740°C for all samples due to decomposition of organic intermediates. Further weight loss between 740°C and 800°C is due to the formation of NASICON phase, that is articulated in DTA plot as sharp exothermic peak. For all samples, weight loss curve follows the same path, but percentage of weight loss is more for 1:3 fuel ratio, since it restrains more carbonaceous material. DTA studies ruled out the plausible structural phase transitions in the material.

Infrared spectroscopy is an important and popular tool for structural exposition and compound identification. Broadband FTIR spectrum in Fig. 3 is of as-prepared material and the bands between 650 and 400 cm^{-1} of calcined powder attribute to harmonics

Table 3

Results of Rietveld refinement of $\text{Na}_3\text{Cr}_2(\text{PO}_4)_3\text{-G1:1}$ sintered at 900°C . The atomic and isotropic displacement factors are obtained from the refinement. R_p (%) = 30.51, R_{wp} (%) = 42.33, $\chi^2 = 3.258$.

Atom	Site	Wyckoff position			$B_{\text{iso}}/\text{\AA}^2$	Occupancy
		x	y	z		
Na(1)	6b	0.0000	0.0000	0.0000	1.448	0.84 (1)
Na(2)	18e	0.655 (3)	0.0000	0.2500	1.409	0.65 (2)
Cr	12c	0.0000	0.0000	0.147 (2)	1.551	1.000
P	18e	0.291 (9)	0.0000	0.2500	2.224	1.000
O(1)	36f	0.181 (5)	−0.039 (7)	0.193 (5)	3.479	1.000
O(2)	36f	0.199 (3)	0.166 (1)	0.0894	1.453	1.000

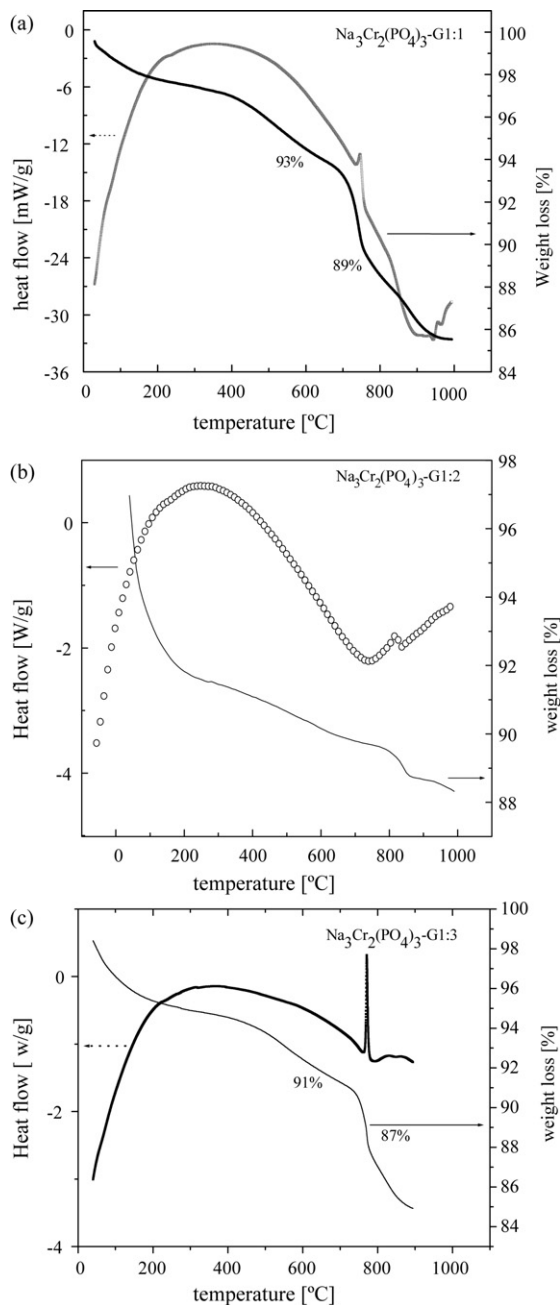


Fig. 2. (a) Thermal and gravimetric analysis of as-prepared $\text{Na}_3\text{Cr}_2(\text{PO}_4)_3\text{-G1:1}$ material in the temperature range of $40\text{--}1000^\circ\text{C}$. (b) Thermal and gravimetric analysis of as-prepared $\text{Na}_3\text{Cr}_2(\text{PO}_4)_3\text{-G1:2}$ material in the temperature range of $40\text{--}1000^\circ\text{C}$. (c) Thermal and gravimetric analysis of as-prepared $\text{Na}_3\text{Cr}_2(\text{PO}_4)_3\text{-G1:3}$ material in the temperature range of $40\text{--}1000^\circ\text{C}$.

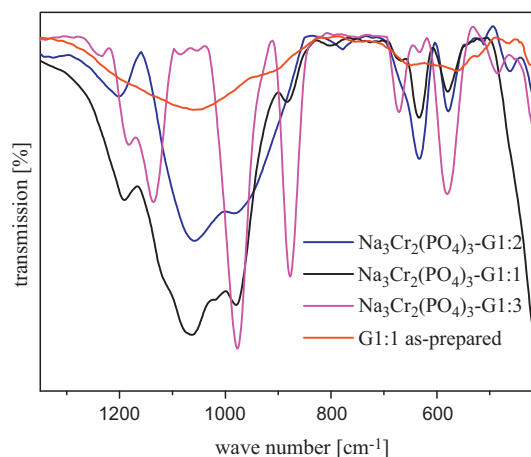


Fig. 3. FTIR spectra of as-prepared and calcined powder of $\text{Na}_3\text{Cr}_2(\text{PO}_4)_3\text{-G1:1}$, $\text{Na}_3\text{Cr}_2(\text{PO}_4)_3\text{-G1:2}$ and $\text{Na}_3\text{Cr}_2(\text{PO}_4)_3\text{-G1:3}$.

of deformation of O–P–O angle (ν_2 and ν_4 modes) [17]. Bands indicated in the region $\sim 560\text{ cm}^{-1}$ are attributed to asymmetric bending vibration modes of O–P–O units [18–20]. Those in the region of $931\text{--}882\text{ cm}^{-1}$ are assigned to PO_3^{2-} ionic group vibration [21]. The region $1250\text{--}900\text{ cm}^{-1}$ is owing to stretching vibrations of PO_4 unit (ν_1 and ν_3 modes) [22]. The interaction of P–O bond and adjacent Cr–O bond is visible in the region of $1227\text{--}1185\text{ cm}^{-1}$ [23]. Vibrational bands confirm the formation of NASICON structure and the spectra shows that there is no change in structure with molar ratio.

UV–vis spectroscopic technique is used to find out the skeleton co-valency of the material, which is related to electronic contribution to electrical conductivity. The UV–vis spectra in Fig. 4 of

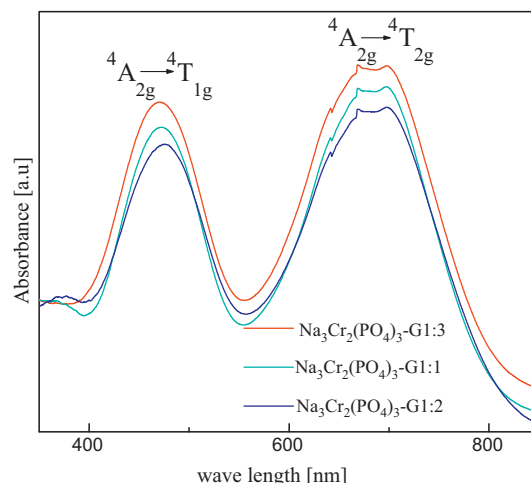


Fig. 4. UV–vis spectrum of $\text{Na}_3\text{Cr}_2(\text{PO}_4)_3\text{-G1:1}$, G1:2 and G1:3.

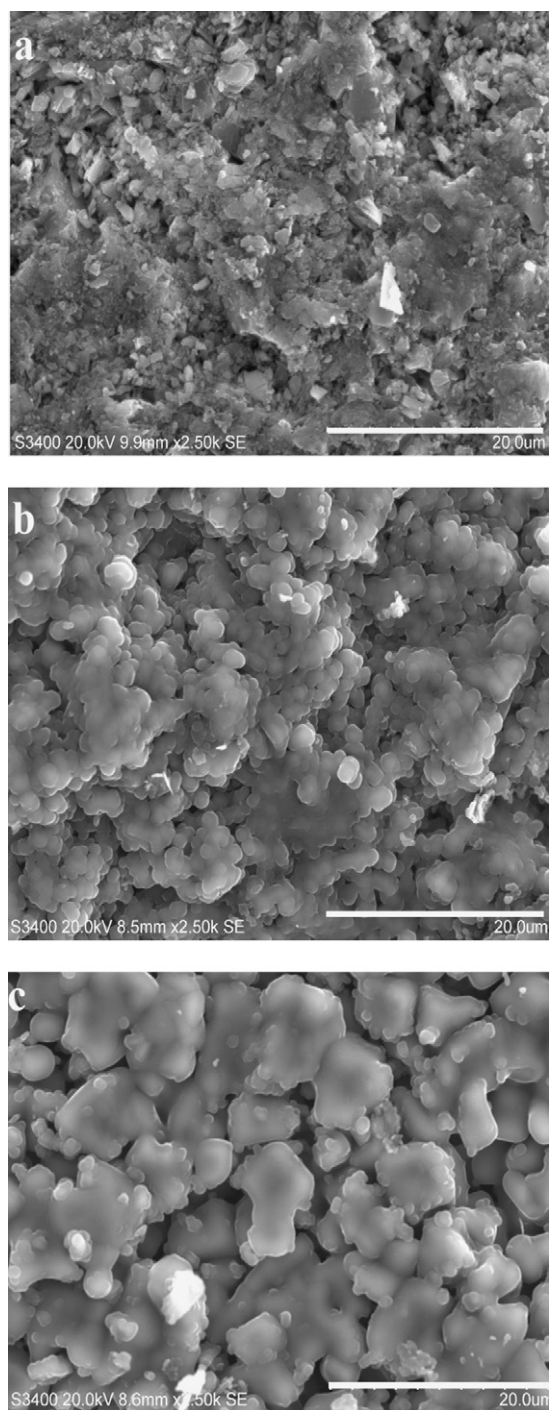


Fig. 5. (a) SEM image of sintered pellet of $\text{Na}_3\text{Cr}_2(\text{PO}_4)_3$ -G1:1. (b) SEM image of sintered pellet of $\text{Na}_3\text{Cr}_2(\text{PO}_4)_3$ -G1:2. (c) SEM image of sintered pellet of $\text{Na}_3\text{Cr}_2(\text{PO}_4)_3$ -G1:3.

$\text{Na}_3\text{Cr}_2(\text{PO}_4)_3$ in different fuel molar ratios show two absorption peaks which signify the octahedral transitions of Cr^{3+} from ground term $^4\text{A}_g$ to two excited quartet terms $^4\text{T}_g$ and $^4\text{T}_{1g}$ [24]. Hence, Na^+ ion is the major conducting species in the $\text{Na}_3\text{Cr}_2(\text{PO}_4)_3$, confirming the material to be of ionic nature in conduction.

Fig. 5(a)–(c) show SEM images of $\text{Na}_3\text{Cr}_2(\text{PO}_4)_3$ material after sintering, synthesized using different fuel ratios. The fuel ratio affects product morphology and sinterability. It is evident from images that density decreases and agglomeration of crystallites increases with fuel ratio. The surface morphology reveals that particles are of submicron size. The nanocrystalline nature of samples is

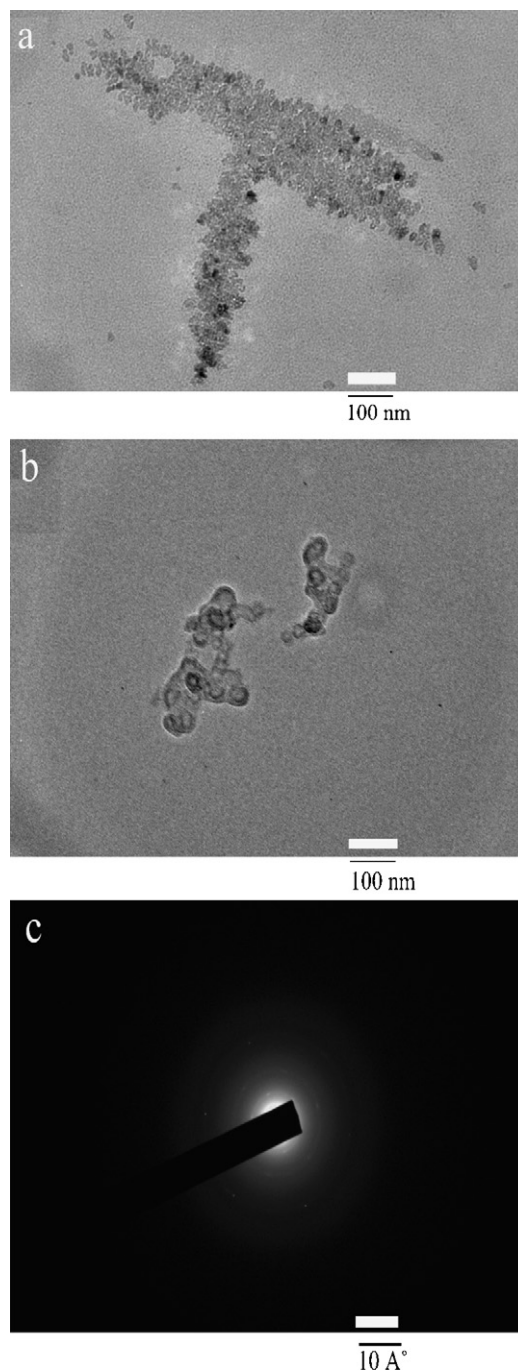


Fig. 6. (a) TEM image of 900 °C sintered $\text{Na}_3\text{Cr}_2(\text{PO}_4)_3$ -G1:1. (b) TEM image of 900 °C sintered $\text{Na}_3\text{Cr}_2(\text{PO}_4)_3$ -G1:3. (c) Diffraction pattern of $\text{Na}_3\text{Cr}_2(\text{PO}_4)_3$ -G1:3.

confirmed from TEM images. Fig. 6(a) and (b) show TEM images of sintered $\text{Na}_3\text{Cr}_2(\text{PO}_4)_3$ -G1:1 and G1:3; the agglomeration of nanometer range crystallites are clear in the images. Fig. 6(c) is the diffraction pattern (seen clearly in the magnified scale) of selected area in the microscopic image of $\text{Na}_3\text{Cr}_2(\text{PO}_4)_3$ -G1:3 of Fig. 6(b). It shows diffraction pattern from different planes of $\text{Na}_3\text{Cr}_2(\text{PO}_4)_3$ -G1:3 with lattice fringes in different orientations. The lattice fringe with d-spacing of 5.37 Å is identified in the image that corresponds to diffraction from $(-3, 1, 2)$ plane, as it is evident from the XRD pattern.

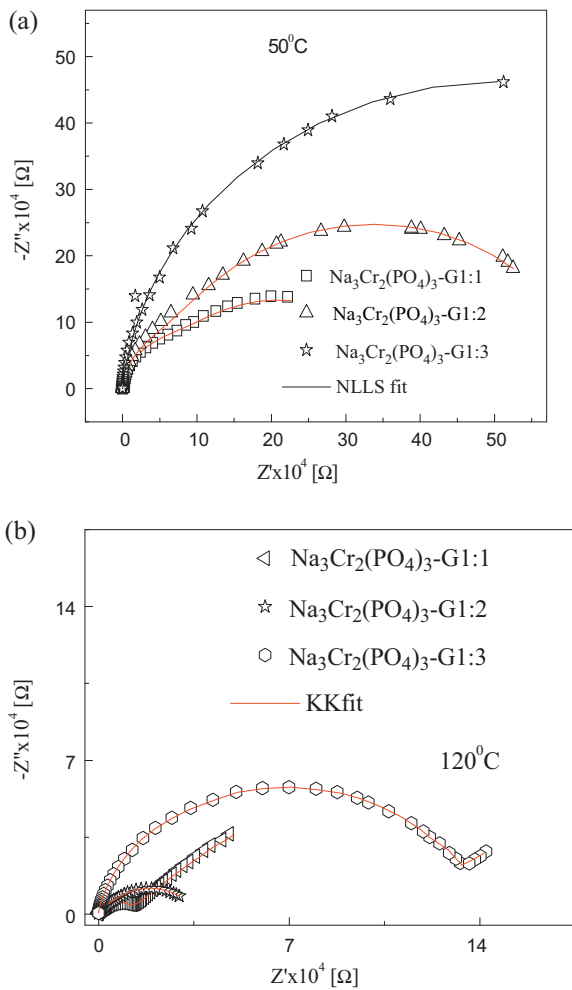


Fig. 7. (a) Complex impedance spectroscopic plot at 50 °C for $\text{Na}_3\text{Cr}_2(\text{PO}_4)_3$ -G1:1, G1:2 and G1:3. The solid line represents NLLS fit to equivalent circuit. (b) Kramers–Kronig fit to complex impedance data measured at 120 °C for $\text{Na}_3\text{Cr}_2(\text{PO}_4)_3$ in different fuel molar ratios achieved through the K–K software test.

The real part, $Z'(\omega)$, and imaginary part, $Z''(\omega)$, of the complex impedance $Z^*(\omega) = Z'(\omega) - iZ''(\omega)$, are calculated from measured G and C as follows:

$$Z'(\omega) = \frac{G}{G^2 + C^2\omega^2} \quad (5)$$

$$Z''(\omega) = \frac{C\omega}{G^2 + C^2\omega^2} \quad (6)$$

where $\omega = 2\pi f$, f being frequency in Hertz. Experimental data is plotted in the complex impedance formalism to extract electrical parameters, namely, grain, grain-boundary resistance, constant phase elements and electrical relaxation time. The impedance investigation of ionic conductors in wide frequency range has advantage because it allows separating the charge transport process in grains and grain-boundaries of ceramics in a wide temperature range. Complex impedance spectra obtained for three fuel ratios at 50 °C is given in Fig. 7(a).

The elements of an equivalent circuit model represent various macroscopic processes involved in the transport of mass and charge. Using non-linear least square fit (NLLS) techniques, all parameters in the equivalent circuit are adjusted simultaneously, thus obtaining optimum fit to the measured dispersion data. A more general NLLS-fit program based on Marquardt algorithm has been used for this process. Impedance parameters are obtained by fitting the data to an equivalent circuit using NLLS fitting procedure

Table 4

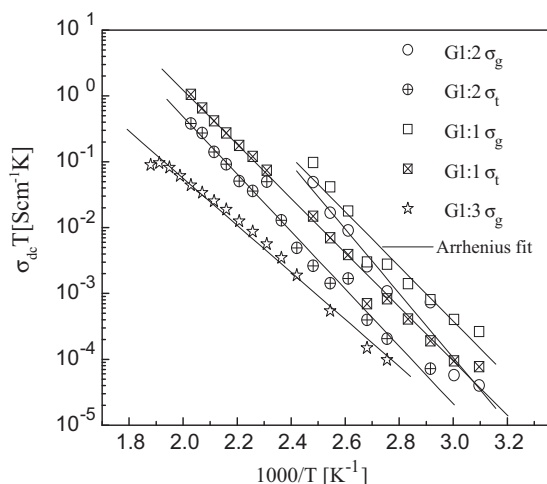
Equivalent circuit and the parameter values at different temperatures for $\text{Na}_3\text{Cr}_2(\text{PO}_4)_3$ in three fuel molar ratios.

$\text{Na}_3\text{Cr}_2(\text{PO}_4)_3$ -G1:1		
Temperature	Equivalent circuit	Parameter values
50	$(R_g Q_g)(R_t Q_t)$	$R_g = 7.59 \times 10^4$, $Q_t = 1.80 \times 10^{-11}$, $n = 0.99$ $R_t = 2.88 \times 10^5$, $Q_g = 1.22 \times 10^{-10}$, $n = 0.91$
60	$(R_g Q_g)(R_t Q_t)(Q_c C_e)$	$R_g = 4.41 \times 10^4$, $Q_g = 2.24 \times 10^{-11}$, $n = 0.98$ $R_t = 1.52 \times 10^5$, $Q_t = 1.64 \times 10^{-10}$, $n = 0.89$ $Q_c = 1.94 \times 10^{-7}$, $n = 0.43$, $C_e = 1.81 \times 10^{-9}$
70	$(R_g Q_g)(R_t Q_t)(Q_c C_e)$	$R_g = 2.30 \times 10^4$, $Q_g = 3.46 \times 10^{-11}$, $n = 0.96$ $R_t = 7.69 \times 10^4$, $Q_t = 1.36 \times 10^{-10}$, $n = 0.92$ $Q_c = 1.81 \times 10^{-7}$, $n = 0.47$, $C_e = 9.68 \times 10^{-10}$
80	$(R_g Q_g)(R_t Q_t)(Q_c)$	$R_g = 8.94 \times 10^3$, $Q_g = 2.68 \times 10^{-11}$, $n = 0.95$ $R_t = 4.52 \times 10^4$, $Q_t = 1.26 \times 10^{-10}$, $n = 0.92$ $Q_c = 9.68 \times 10^{-7}$, $n = 0.51$
90	$(R_g Q_g)(R_t Q_t)(Q_c)$	$R_g = 3.75 \times 10^3$, $Q_g = 1.96 \times 10^{-11}$, $n = 0.99$ $R_t = 1.73 \times 10^4$, $Q_t = 1.39 \times 10^{-10}$, $n = 0.92$ $Q_c = 1.96 \times 10^{-7}$, $n = 0.56$
100	$(R_g Q_g)(R_t Q_t)(R_c C_e)$	$R_g = 1.66 \times 10^3$, $Q_g = 2.78 \times 10^{-11}$, $n = 0.98$ $R_t = 9.84 \times 10^3$, $Q_t = 2.27 \times 10^{-10}$, $n = 0.90$ $R_c = 3.78 \times 10^5$, $Q_c = 2.21 \times 10^{-7}$, $n = 0.57$
$\text{Na}_3\text{Cr}_2(\text{PO}_4)_3$ -G1:2		
50	$(R_g Q_g)(R_t Q_t)$	$R_g = 2.65 \times 10^4$, $Q_t = 2.58 \times 10^{-11}$, $n = 0.99$ $R_t = 5.73 \times 10^5$, $Q_g = 1.09 \times 10^{-10}$, $n = 0.89$
60	$(R_g Q_g Q_g)(R_t Q_t)$	$R_g = 2.16 \times 10^4$, $Q_g = 3.39 \times 10^{-11}$, $n = 0.96$ $R_t = 1.12 \times 10^5$, $Q_t = 5.26 \times 10^{-10}$, $n = 0.83$
70	$(R_g Q_g)(R_t Q_t)$	$R_g = 4.71 \times 10^4$, $Q_g = 3.19 \times 10^{-11}$, $n = 0.96$ $R_t = 2.14 \times 10^5$, $Q_t = 3.66 \times 10^{-10}$, $n = 0.86$
80	$(R_g Q_g)(R_t Q_t)$	$R_g = 2.13 \times 10^4$, $Q_g = 3.29 \times 10^{-10}$, $n = 0.96$ $R_t = 1.12 \times 10^5$, $Q_t = 5.38 \times 10^{-10}$, $n = 0.83$
90	$(R_g Q_g)(R_t Q_t)$	$R_g = 5.10 \times 10^3$, $Q_g = 1.66 \times 10^{-10}$, $n = 0.99$ $R_t = 2.74 \times 10^4$, $Q_t = 1.22 \times 10^{-10}$, $n = 0.87$
100	$(R_g Q_g)(R_t Q_t)$	$R_g = 2.82 \times 10^3$, $Q_g = 4.04 \times 10^{-11}$, $n = 0.98$ $R_t = 3.32 \times 10^4$, $Q_t = 1.08 \times 10^{-9}$, $n = 0.77$
$\text{Na}_3\text{Cr}_2(\text{PO}_4)_3$ -G1:3		
50	$(R_g Q_g)$	$R_g = 1.02 \times 10^6$, $Q_g = 3.24 \times 10^{-11}$, $n = 0.93$
60	$(R_g Q_g)$	$R_g = 6.63 \times 10^5$, $Q_g = 2.03 \times 10^{-11}$, $n = 0.96$
70	$(R_g Q_g)$	$R_g = 3.66 \times 10^5$, $Q_g = 3.71 \times 10^{-11}$, $n = 0.93$
80	$(R_g Q_g)$	$R_g = 4.51 \times 10^5$, $Q_g = 3.11 \times 10^{-11}$, $n = 0.94$
90	$(R_g Q_g)$	$R_g = 2.86 \times 10^5$, $Q_g = 4.10 \times 10^{-11}$, $n = 0.93$
100	$(R_g Q_g)$	$R_g = 1.29 \times 10^5$, $Q_g = 5.14 \times 10^{-11}$, $n = 0.92$

Table 5

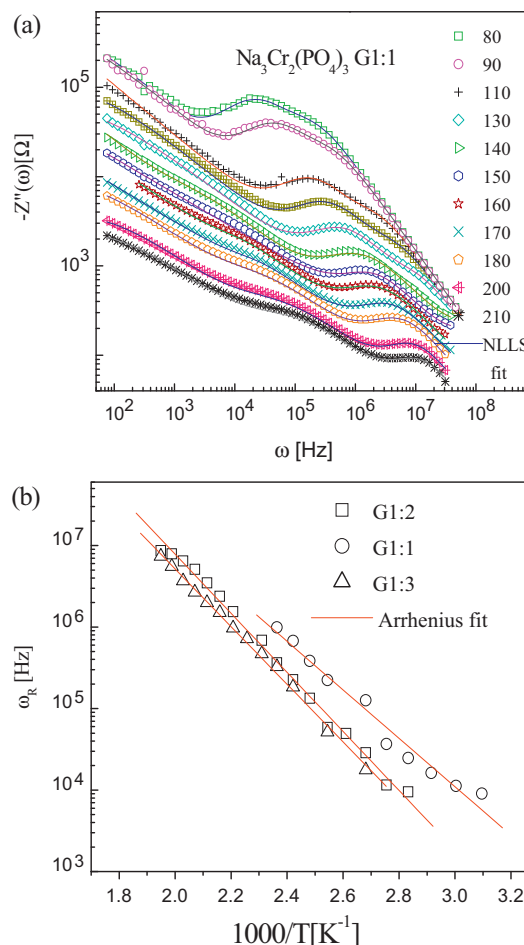
Grain and total dc conductivities calculated from complex impedance representation and activation energies of dc conduction and dispersion peak frequency.

Sample	dc conductivity		Activation energy (eV)		
	at 50 °C (S cm ⁻¹)		complex impedance		
	Grain (σ_{dcg})	Total (σ_{dct})	Grain	Total	Z'' peak
NCP-G1:1	$(2.35 \pm 0.25) \times 10^{-6}$	$(5.57 \pm 0.69) \times 10^{-7}$	(0.82 ± 0.07)	(0.81 ± 0.02)	(0.59 ± 0.03)
NCP-G1:2	$(2.13 \pm 0.25) \times 10^{-6}$	$(2.10 \pm 0.32) \times 10^{-7}$	(0.97 ± 0.08)	(0.87 ± 0.03)	(0.61 ± 0.01)
NCP-G1:3	$(1.75 \pm 0.15) \times 10^{-7}$	–	(0.71 ± 0.02)	–	(0.70 ± 0.01)

**Fig. 8.** Arrhenius plot of dc conductivity values obtained from impedance representation. Solid line is Arrhenius fit to the experimental values.

due to Boukamp [25,26]. Except for $\text{Na}_3\text{Cr}_2(\text{PO}_4)_3$ -G1:3 [27], equivalent circuit consists of a depressed semi-circle, ($R_g Q_g$) that stands for grain contribution and part of another semi-circle, ($R_t Q_t$), which represents total contribution from grain and grain-boundary in the low-frequency region. Impedance plane plots are depressed due to distribution of relaxation times; a non-ideal capacitor or constant phase element, Q , is used to explain the depression [28]. R_g and R_t of samples are obtained by intercept of high frequency and low frequency semi-circles with real axis and is used to calculate dc conductivity values, σ_{dcg} and σ_{dct} using the cell constant. Table 4 gives the equivalent circuit and its parameter values at different temperatures for $\text{Na}_3\text{Cr}_2(\text{PO}_4)_3$ in three fuel molar ratios.

Kramers–Kronig (K–K) relation is used to check the quality of impedance data. Validity of these relations depends on linearity, causality and stability of impedance spectroscopic data. The real part of a spectrum can be obtained by integration of imaginary part and vice versa. If the measured complex data do not obey K–K relations, data must violate one of the conditions. K–K transform requires integration over a range of frequency from zero to infinity. Since no one can measure frequency over that range, evaluating the K–K relations via integration always involves assumptions about the behavior of a spectrum outside the frequency over which it was measured. Practically, K–K analysis is performed by fitting a generalized model to spectral data. Agarwal et al. [29] proposed a model, which consists of m number of serially connected Voigt elements: $R(RC)_m$, where m is the number of complex plane data points in the spectrum. By definition this model is K–K compliant. Boukamp [30], proposed a method through linear equations by eliminating probable non-convergence issues. K–K fit to the complex impedance data of $\text{Na}_3\text{Cr}_2(\text{PO}_4)_3$ in different fuel molar ratios at 120 °C using the software K–K test is shown in Fig. 7(b). This software is based on Boukamp's model [31] and the fit matches well with experimental data implying the good quality of data for all fuel ratios.

**Fig. 9.** (a) Dispersion of $Z''(\omega)$ of $\text{Na}_3\text{Cr}_2(\text{PO}_4)_3$ -G1:1 at different temperatures. (b) Arrhenius fit to dispersion peak frequency (ω_R) at different temperatures.

At 50 °C magnitudes of Q_g and Q_t are found to be $(1.80 \times 10^{-11} \pm 5.73\%) \text{S} \cdot \text{s}^n$ and $(1.22 \times 10^{-10} \pm 3.75\%) \text{S} \cdot \text{s}^n$ for $\text{Na}_3\text{Cr}_2(\text{PO}_4)_3$ -G1:1, this implies that Q_g and Q_t are grain and grain-boundary contributions, respectively. The parameters σ_{dcg} and σ_{dct} are thermally activated and shows Arrhenius dependence on temperature and it is given by:

$$\sigma_{dc} T = \sigma_0 \exp \left(-\frac{E_\sigma}{k_B T} \right) \quad (7)$$

where σ_{dc} is the dc conductivity, σ_0 is the pre-exponential factor, T is the temperature in Kelvin, E_σ is the activation energy for dc conduction and k_B is the Boltzmann's constant. The dc conductivity values and activation energy obtained from slope of Arrhenius plot are given in Table 5. Arrhenius plot of dc conductivity values, σ_{dcg} and σ_{dct} , obtained for three fuel molar ratios are shown in Fig. 8. The highest dc conductivity value is found for $\text{Na}_3\text{Cr}_2(\text{PO}_4)_3$ -G1:1 and its magnitude is one order higher than the reported value of $1.17 \times 10^{-7} \text{S cm}^{-1}$, for conventionally synthesized material [3].

The present study shows that grain and total conductivity decreases with fuel ratio and is quite dependable on the material's density. Least conductivity of the fuel rich molar ratio is due to its low density and large crystallite size.

Characteristic relaxation frequencies for the grain are obtained from the peak of imaginary part of the impedance spectrum. The dispersion curves in Fig. 9(a) of $\text{Na}_3\text{Cr}_2(\text{PO}_4)_3\text{-G1:1}$ show high frequency grain and low frequency grain-boundary contributions. Frequency of relaxation (ω_R) exponentially increases with temperature and its activation energy, E_R , is obtained from Arrhenius plot in Fig. 9(b), and its value is given in Table 5. This illustrates that while relaxing, ions have to overcome less energy barrier compared to the conducting process.

Transport number measurement is done by Wagner's polarization technique. In this method a constant dc voltage of 400 mV is applied to the sample between a pair of silver blocking electrodes [32]. The configuration is maintained at 250 °C for 2 h for temperature stabilization and on application of voltage, the instantaneous initial current, I_0 , is 14 μA . After 48 h the cell is completely polarized and delivers a steady current, I_s , of 0.19 μA , further there is no change in this steady current with time. Decrease in polarization current can be attributed to the migration of ions due to applied field and is balanced by diffusion due to the concentration gradient. Thus, the resulting steady-state current is due to electrons or holes, and its contribution is 0.01. The ion transport number is evaluated by the equation [33],

$$t_i = 1 - \frac{I_s}{I_0} \quad (8)$$

which is found to be nearly equal to unity.

4. Conclusions

By novel solution combustion method $\text{Na}_3\text{Cr}_2(\text{PO}_4)_3$ nano-crystallites are synthesized for the first time in a stable rhombohedral phase. The effect of glycine fuel molar ratio on physical and ac electrical properties of the material are investigated. Compared to the conventional methods, this technique saves time, energy and turns to be effective for producing phase pure material in nano-crystalline form. XRD, FTIR, TG-DTA and SEM/TEM techniques confirm the phase formation of the material. Rietveld refinement of room temperature XRD unveils $\text{Na}_3\text{Cr}_2(\text{PO}_4)_3$ structure to be of rhombohedral phase with $R\bar{3}c$ space group. It is observed that the lattice parameters and crystallite size are reliable on fuel ratio. As the fuel ratio increases, agglomeration increases due to hike in the flame temperature. The agglomeration decreases density owing to less packing of larger crystallites, which affects the electrical properties adversely. UV–vis spectroscopy and dc polarization techniques are utilized to confirm the ionic nature of conducting species. Among the synthesized materials $\text{Na}_3\text{Cr}_2(\text{PO}_4)_3\text{-G1:1}$ show the highest conductivity that is an order

of magnitude higher than the reported value. This study concludes that, the fuel molar ratio play a major role in deciding physical and electrical properties and 1:1 is the optimized ratio in this study. These materials could find possible application in gas sensors due to its thermal stability and high ion conductivity.

Acknowledgements

Financial support from DST research project no. SR/S2/CMP-61/2006 and UGC research project no. 33-32/2007 (SR) is gratefully acknowledged and LV would like to thank DST for JRF. Authors would like to acknowledge the UGC Special Assurances Programme F.530/15/DRS/2009 (SAP-I) for the financial support. Authors would like to thank Central Instrumentation Facility (CIF), Pondicherry University for SEM, DTA-TG and FTIR facilities. Dr. G. Saini, AIRF, JNU, New Delhi is acknowledged for providing TEM image.

References

- [1] H.Y.-P. Hong, Mater. Res. Bull. 11 (1976) 173.
- [2] J.B. Goodenough, H.Y.-P. Hong, J.A. Kafalas, Mater. Res. Bull. 11 (1976) 173.
- [3] F. d'Yvoire, M. Pintard-ScrGpell, E. Bretey, M. de la Rochsre, Solid State Ionics 9–10 (1983) 851.
- [4] A. Martucci, S. Sartori, M. Guglielmi, M.L. Di Vona, S. Licocchia, E. Traversa, J. Eur. Ceram. Soc. 22 (2002) 1995.
- [5] L. Silvia, M.L. Di Vona, T. Enrico, M. Laura, J. Eur. Ceram. Soc. 19 (1999) 925.
- [6] S. Youichi, A. Yasunori, M. Satoko, Mater. Chem. 7 (1997) 1487.
- [7] M.L. Di Vona, T. Enrico, L. Silvia, J. Sol Gel Sci. Technol. 19 (2000) 463.
- [8] N. Arul Dhas, K.C. Patil, J. Mater. Chem. 5 (1995) 1463.
- [9] X. Dong, Z. Wu, X. Chang, W. Jin, N. Xu, Ind. Eng. Chem. Res. 46 (2007) 6910.
- [10] R.D. Purohit, S. Saha, A.K. Tyagi, J. Nucl. Mater. 288 (2001) 7.
- [11] L.E. Shea, J. McKittrick, O.A. Lopez, E. Sluzky, J. Am. Ceram. Soc. 79 (1996) 3257.
- [12] G.K. Williamson, W.H. Hall, Acta Metall. 1 (1953) 22.
- [13] T. Ye, Z. Guiwen, Z. Weiping, X. Shangda, Mater. Res. Bull. 32 (1997) 501.
- [14] H. Hahn, J. Logas, R.S. Averback, J. Mater. Res. 5 (1990) 609.
- [15] B.H. Toby, J. Appl. Crystallogr. 34 (2001) 210.
- [16] A.C. Larson, R. B. Von Dreele, Los Alamos National Laboratory Report LAUR 1994, 86 pp.
- [17] K.J. Rao, K.C. Sobha, S. Kumar, Proc. Indian Acad. Sci. 113 (2001) 497.
- [18] A.A. Higazy, B. Bridge, J. Mater. Sci. 20 (1985) 2345.
- [19] C. Dayanand, G. Bhikshaiah, V. Jayatyagaraju, M. Salagram, A.S.R. Krishnamurthy, J. Mater. Sci. 31 (1996) 1945.
- [20] I.N. Chakraborty, R.A. Condrate, Phys. Chem. Glasses 26 (1985) 68.
- [21] M. Sayer, A. Mansingh, Phys. Rev. B 6 (1972) 4629.
- [22] D.E.C. Corbridge, E.J. Lowe, J. Chem. Soc. 78 (1954) 493.
- [23] J. Alamo, R. Roy, J. Mater. Sci. 21 (1986) 444.
- [24] C. Delmas, F. Cherkaoui, P. Hagenmuller, Mater. Res. Bull. 21 (1986) 469.
- [25] B.A. Boukamp, Equivalent circuit-EQUIVCRT Program, version 4.55, University of Twente, Holland, 1997.
- [26] Lakshmi Vijayan, G. Govindaraj, Phys. B: Condens. Matter 404 (2009) 3539.
- [27] Lakshmi Vijayan, R. Cheruku, G. Govindaraj, S. Rajagopan, Mater. Chem. Phys. 125 (2011) 184.
- [28] E. Barsoukov, J.R. Macdonald, Impedance Spectroscopy Theory, Experiment, and Applications, second ed., John Wiley & Sons, New Jersey, 2005.
- [29] P. Agarwal, M.E. Orazem, L.H. Garcia-Rubio, J. Electrochem. Soc. 139 (1992) 1917.
- [30] B.A. Boukamp, J. Electrochem. Soc. 142 (1995) 1885.
- [31] B.A. Boukamp, Solid State Ionics 169 (2004) 65.
- [32] J. Schoonman, F.G. Dijkman, J. Solid State Chem. 5 (1972) 111.
- [33] N. Srivastava, A. Chandra, S. Chandra, Phys. Rev. B 52 (1995) 225.